

---

## DELIVERABLE

---

### WP 28, Task 3: Report on real-time inversion methods for kinematic rupture parameter estimation

<b>Work package</b>	28,3: Report on real-time inversion methods for kinematic rupture parameter estimation
<b>Lead</b>	CNRS
<b>Authors</b>	[Bertrand Delouis, CNRS] [Françoise Courboulex, CNRS] [Stefania Tarantino, UNINA] [Simona Colombelli, UNINA] [Antonio Scala, UNINA] [Antonio Emolo, UNINA] [Gaetano Festa, UNINA] [Antonio Scala, UNINA]
<b>Reviewers</b>	[Fabrice Cotton, GFZ]
<b>Approval</b>	[Management Board]
<b>Status</b>	[Final]
<b>Dissemination level</b>	[Public]
<b>Delivery deadline</b>	[31.10.2019]
<b>Submission date</b>	[31.10.2019]
<b>Intranet path</b>	[e.g. DOCUMENTS/DELIVERABLES/File Name]



## Table of Contents

1	Summary .....	3
2	Motivation and challenges.....	3
3	Data .....	4
3.1	Forward modelling for synthetic data computation.....	4
3.2	Source modelling and the Green’s tractions .....	5
3.3	Data Processing and Data Selection for the SLIPNEAR method .....	7
3.4	Data processing for Back-Projection .....	8
4	Algorithms .....	8
4.1	SLIPNEAR .....	8
4.1.1	Kinematic models and inversion.....	9
	Average slip model.....	11
	Model discrepancy.....	11
	Index of confidence on the stability of the slip map .....	12
	Index of confidence on the discrimination of the rupture plane.....	12
4.2	Back-Projection .....	12
5	Results .....	13
5.1	SLIPNEAR .....	13
5.2	Back-Projection .....	20
5.3	Final remarks about back projection method.....	27
6	Conclusions and perspectives.....	28
7	References .....	30

## 1 Summary

---

The present document summarizes the activities and the main results of task 28.3. Within this task we explored two different strategies for the rapid estimation of the earthquake source models, using the P and S-wave recordings, as they are progressively available at the recording near-source stations. The final goal is to use these refined, kinematic source models for the computation of synthetic seismograms and shake maps, with the aim of reducing the uncertainties on the ground shaking prediction. The two approaches presented here are expected to provide complementary images of the source and independent estimates of different parameters involved in the rupture process.

We first present the technical details of the two methods and then show the performance of their application to synthetic and real earthquake data, separately. Finally, we discuss advantages and limitations of the two approaches and hypothesize how the two methods could be combined to get a refined and complete-frequency source description.

## 2 Motivation and challenges

---

The goal is to design and develop refined methods for the real-time or near real-time inverse/forward modelling of the kinematic rupture, in which the geometry and extension of the source are mapped and continuously updated to reconstruct the fault slip history from the signals and to predict the space-time ground shaking evolution. In real-time and near real-time applications, the source is typically described with a point source approximation, often providing unrealistic ground shaking distributions. The inversion for the static slip on the fault plane, allows indeed consideration of the contributions from the entire rupture plane and may provide a better estimation of the earthquake magnitude. The ambitious target here is to prefigure a real-time alert system operating in the region surrounding the area of earthquake nucleation, based upon a “quake-shaking forecast” system, analogous to the weather forecasting system, but acting at an extremely smaller time scale (seconds to minutes). The forecast system will assimilate the continuous waveform data streaming collected by a dense network of spatially distributed probes and will output the space-time evolutionary images of the ground shaking, physically related to the ongoing propagating earthquake source.

In this perspective view, the time evolution of the initial P-wave signals will be analyzed both to provide stable geometrical constraints for near-real time inversion techniques and to determine the evolutionary rupture kinematic model, as progressively enlarged P-wave time windows become available during the earthquake process.

In particular, our purposes are to:

- Develop and test methods of kinematics inversion in real-time or near real-time, which will provide information about the extended character of the earthquake source that can be incorporated into ShakeMaps;
- Develop and apply back-projection techniques for the determination of the rupture velocity and for the rapid location of high-frequency slip patches during the earthquake rupture process;
- Develop real-time, automatic & evolutionary methods of source imaging with inclusion of synthetic seismograms to refine the shake-maps;

- Characterize refined seismic source including high-frequency images of the source process to reduce the uncertainties and improve the ground shaking prediction.

## 3 Data

---

We used two inversion techniques, hereinafter referred to as SLIPNEAR and Back-Projection respectively. We tested the performance using both synthetic and real earthquake data. In particular, for both techniques, the use of synthetic data allowed for the direct comparison of the inverted source with the simulated source description. The presented synthetic data-set refer to the case study of the Norcia earthquake (2016/10/30, Mw=6.5) occurred during the 2016 Central Italy sequence.

### 3.1 Forward modelling for synthetic data computation

---

The synthetic data are obtained exploiting the discrete formulation of the following seismic source representation integral, that expresses the seismogram at the location  $\mathbf{x}$  on the Earth's surface as the convolution of a source term located at  $\boldsymbol{\xi}$  with the elastic response of the medium propagation

$$u_m(\mathbf{x}, t) = \int_{-\infty}^{+\infty} d\tau \int_{\Sigma} \delta u_i(\boldsymbol{\xi}, t) c_{ijkl} n_j \frac{\partial G_{mk}}{\partial \xi_l}(\mathbf{x}, t - \tau; \boldsymbol{\xi}) d\xi \quad (2.1)$$

where  $\mathbf{c}$  is the elastic coefficients tensor and  $G_{mk}$  represents the m-th component of the displacement recorded at the position  $\mathbf{x}$  at the time  $t$  due to an impulsive force in the k-th direction, at  $\boldsymbol{\xi}$  and at the time 0.

The eq. (2.1) can be manipulated to represent the extended source as a superposition of double-couple point sources and expressed in the frequency domain as follows:

$$u_m(\mathbf{x}, \omega) = \int_{\Sigma} \delta \mathbf{u}(\boldsymbol{\xi}, \omega) \cdot \mathbf{T}_m^G(\mathbf{x}, \omega; \boldsymbol{\xi}) d\xi \quad (2.2)$$

where  $\mathbf{T}_m^G(\mathbf{x}, \omega; \boldsymbol{\xi})$  is generally referred to as Green's traction and is a term that incorporates the elastic coefficients tensor and the normal projection to the surface. Once the geometry of the fault rupture is defined, the source term in eq. (2.2) is the representation in the frequency domain of the following factorization:

$$\delta \mathbf{u}(\boldsymbol{\xi}, t) = A(\boldsymbol{\xi}) S(t - T_R(\boldsymbol{\xi}); \tau(\boldsymbol{\xi})) \mathbf{r}(\boldsymbol{\xi}) \quad (2.3)$$

the term  $A$  represents the final amplitude of the slip and  $S$  is the function describing the slip increases from zero at the activation time  $T_R$  to  $A$  at  $T_R + \tau$ , with  $\tau$  being the rise time. Finally, the unit vector  $\mathbf{r}$  is the slip direction.

For our application the source has been discretized in  $N$  equally spaced sub-sources, hence the eq. (2.2) assumed the following discrete form:

$$\mathbf{u}(\mathbf{x}, \omega) = \sum_{i=1}^N A_n \hat{S}(\omega, \tau_n) e^{-i\omega T_{Rn}} \mathbf{r}_n \cdot \mathbf{T}_n^G(\mathbf{x}, \omega) \quad (2.4)$$

More details about the formulation and its discrete representation can be found in Festa & Zollo (2012).

## 3.2 Source modelling and the Green's tractions

To model and discretize a Norcia-like source description as discussed in the previous sub-section we used the fast source parameter estimates already presented in the deliverable 28.1 and published in several recent research paper (Bose et al., 2018; Tarantino et al., 2019; Nazeri et al., 2019).

The expected length along the strike direction of the rupture model was inferred from the *FinDer* estimates as already described in the sections 2.1 and 3.1 of the deliverable 28.1 (see also Böse *et al.* 2012, 2015 and 2018). The results of this algorithm, for the Norcia earthquake, showed a convergence to the expected length from Wells & Coppersmith (1994) scaling law (Figure 3.1.2 in deliverable 28.1). This quantity, hereinafter referred to as length  $L$  is hence imposed to 26.3 km.

Fast estimates of the rupture extension were computed for the main events of central Italy 2016 sequence by analyzing the variation of the peak kinematic quantities within the P-wave window. (deliverable 28.1 sections 2.2 and 3.2 Activity 1; see also Nazeri *et al.* 2019). These estimates can be interpreted as the radius of the main patch of fault slip for events as large as the Norcia earthquake and hence they can be used to constrain the smaller dimension of a rectangular fault plane model, that is the width  $W$  (Wells & Coppersmith, 1994). For the case-study the estimated radius is 5.04 km (Nazeri *et al.* 2019) and therefore we imposed  $W=10.08$  km.

Finally, the focal mechanism was constrained by exploiting the results of the algorithm presented in Tarantino *et al.* (2019, see also deliverable 28.1 sections 2.2 and 3.2 Activity 2). For the analyzed case-study, in an off-line test, this method provided the following stable solution for the focal mechanism after 7.7 seconds: strike = 155°, dip = 56°, rake = -95°.

Starting from the available estimates, a rectangular fault plane oriented according to the focal mechanism with dimensions  $2L \times W$  has been built. The fault plane is centered on the hypocenter of the case-study. The doubled length of the fault plane allows to place in a random position the main patch of slip. A sketch of the fault projection onto the Earth's surface is shown in Figure 2.2.1(a).

The fault has been discretized in 23936 sub-sources in a 150 m spaced regular grid. Considering a rupture propagating at  $\sim 3$  km/s, this would allow to model the generated signal up to  $\sim 4$  Hz properly describing the smallest wavelength with at least 5-6 point. An inhomogeneous rise-time has been imposed on the sub-sources and each of the rise time value has been extracted from a Gaussian distribution having a mean of 0.6 s; the rupture velocity is fixed at 2.7 km/s that is  $\sim 80\%$  of the of the S-wave velocity in the medium. A linear ramp has been implemented as source function. The justification to these choices can be found in Scala *et al.* (2018).

Finally, the slip amplitude distribution  $A$  has been defined, over a length  $L$ , summing a low-frequency Gaussian model (figure 2.2.1(a) top), to model the main slip patch, and a stochastic  $k^2$  distribution (Herrero & Bernard, 1994; Scala *et al.* 2018) to model the shorter wavelength source contributions (figure 2.2.1(a) middle). The center of the Gaussian slip is randomly extracted from a uniform distribution and the other sub-sources having  $A \neq 0$  are located at a distance  $d \leq L/2$  with respect to this center. In figure 2.2.1(a - bottom) the final stochastic slip distribution is shown. In figure 2.2.1(b) the final slip distribution is shown on the projection onto the Earth's surface.

The synthetic seismograms were computed assuming a 1-D velocity model for wave propagation (Bianchi et al., 2010 modified by Ameri et al., 2012). This allows to efficiently compute the Green's traction in the frequency domain solving the wave propagation equation through the reflectivity method. This approach is efficiently implemented in the AXITRA code ([axitra.tar.gz](http://axitra.tar.gz)) and in the first part of the LinSlipInv code (<http://fgallovic.github.io/LinSlipInv/>).

The synthetic seismograms were computed at the location of 51 real stations that recorded the Norcia event. The epicenter of the event (red star) and the stations (green triangles) are plotted in Fig. 2.2.1(b).

The three-component signal at the stations T1220, and AMT (see the text within the figure 2.2.1(b)) are showed in figure 2.2.1(c-d). With respect to the main patch of the slip, they represent the synthetic velocity traces at a directive and an anti-directive station, respectively.

Finally, in figures 2.2.1(e-f) the amplitude displacement spectra for the same stations in the panels (c-d) are plotted for the vertical component. The corner frequency ranges from 0.15 to 0.35 for the stations considered in the analysis.

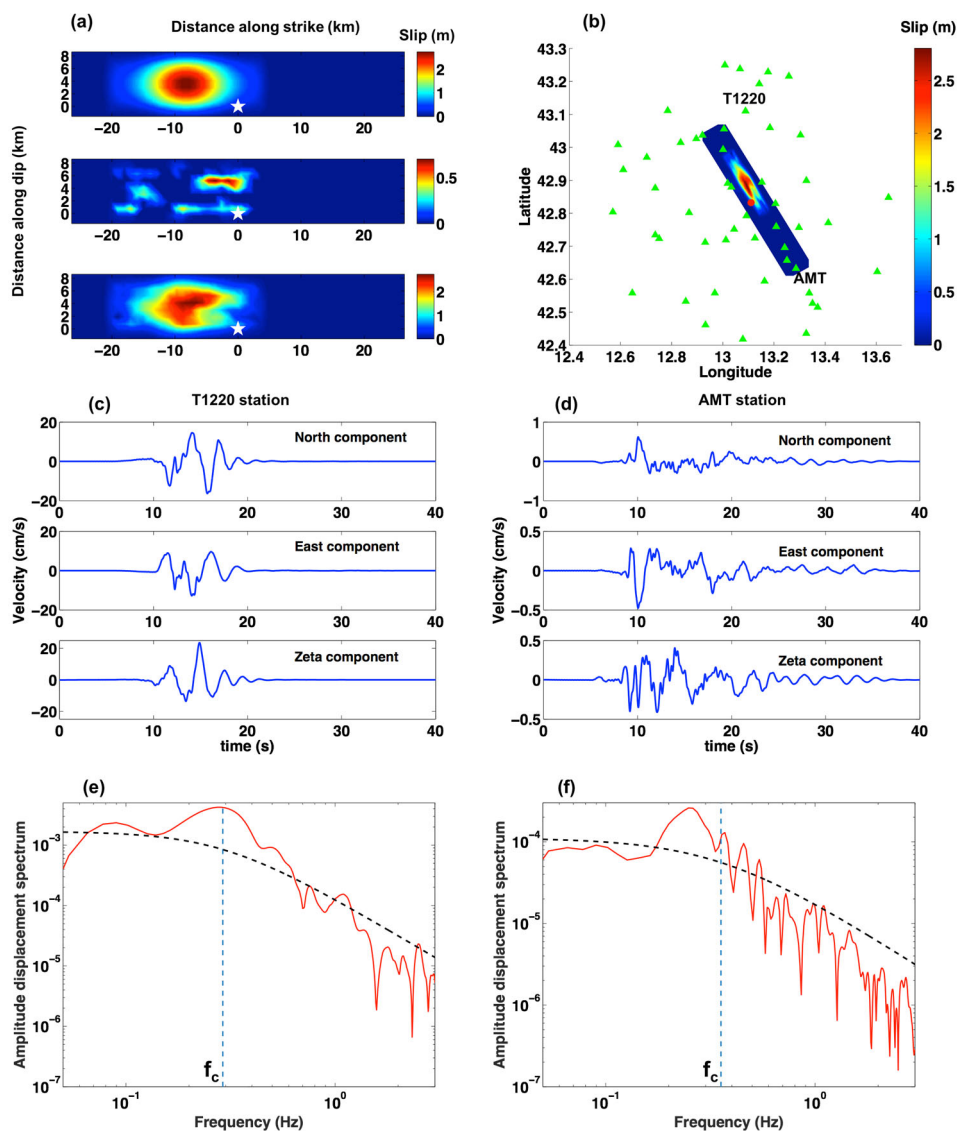


Figure 2.2.1 (a) Scheme of the  $k^{-2}$  modelling of the source: on the top the Gaussian low frequency distribution, in the middle the stochastic distribution of the shorter wavelength slip asperities, on the bottom the final model as the summation of the low and high frequency descriptions. (b) Projection onto the Earth's surface of the fault plane used in the forward model. On the fault projection the slip

distribution is plotted. The red dot and the green triangles represent the epicenter and the used stations respectively. The texts refer to the stations whose synthetic traces are plotted in the panels (c) and (d). (e-f): the amplitude displacement spectra for the same stations of panel (c) and (d). The spectra are inverted through a classical  $f^{-2}$  fit (black dashed lines) and the corner frequencies are extracted (blue dashed lines).

### 3.3 Data Processing and Data Selection for the SLIPNEAR method

---

Data processing for the SLIPNEAR method is similar to that of the FMNEAR approach (Delouis, 2014). It comprises removing the pre-event baseline offset, picking the initial P-wave arrival, doubly integrating the acceleration time series to obtain displacement, windowing, time shifting, band-pass filtering, and decimation. For the testing phase, the first P-wave arrival times are manually picked onto the vertical component but for near-real time applications the P waves are picked automatically.

To get rid of contaminated low frequencies, an adapted high-pass filter is applied. We addressed this question in detail in Delouis, Charlety, and Vallée (2009), for the automated computation of Mw (MWSYNTH method) and the same approach is used in the FMNEAR approach (Delouis, 2014). Briefly, we analyze the acceleration spectrum of the whole seismic signal and identify deviations from the expected linear trend of positive slope at low frequency.

The high-pass (i.e., low-cut) frequency ( $f_{min}$ ) is identified as the frequency from which the acceleration spectrum maintains a positive near-constant slope up to the plateau area near the corner frequency. As a result, the  $f_{min}$  values may be different for the three components of a same station. On the other hand, the low-pass (i.e., high-cut) frequency ( $f_{max}$ ) is predetermined as a function of magnitude, on the basis of a series of test inversions performed with a series of benchmark earthquakes.  $f_{max}$  decreases with magnitude (M), from 0.15 Hz for  $M < 6.5$  to 0.1 Hz for  $M > 8.5$ , and is also adjusted as a function of distance. We end up with boundary frequencies  $f_{min}$  and  $f_{max}$ , which define the filtering band pass for individual components (north–south, east–west, and vertical).

A special attention is used to identify saturated or tilted broadband seismograms, that have to be discarded or used only partially keeping only the initial part before saturation or tilting.

Since the desired goal is the near real-time implementation, the number of stations to be incorporated in the inversion is limited by optimizing their azimuth – distance distribution. The region around the epicenter is subdivided into 48 sectors of azimuth and distance, and we initially select a maximum of one station per sector, avoiding using groups of closely located stations. Then, we fix the minimum number of selected stations to 15, and the maximum to 28. Data processing is fully automated so that it is usable for near real-time implementation.

#### **Note regarding High rate GPS data**

In the description of Task 3 it was initially considered to include High Rate GPS data as complementary input for the kinematic slip inversion. In regard to the fact that real-time processing of high rate GPS data is experimented in a very few places only, and that there remain issues to be resolved to obtain static displacement or time series in real time with a sufficient degree of confidence, we decided to concentrate our efforts on consolidating the inversion of seismological data alone and on the testing of the methodology in near real time at the world wide scale. Testing the approach in near-real time was not proposed in the initial description of Task 3, but we believe it is the most useful extension of our work considering that the real time access of seismological data is easy and well organized through Federation of Digital Seismograph Networks (fdsn) web services.

## 3.4 Data processing for Back-Projection

---

Our Back-Projection approach can be considered as an extension of the technique proposed by Maercklin et al. (2012) to a near source application. We use vertical component as in Maercklin et al. (2012), and compute the SV radiation pattern for each sub-source/receiver couple.

In an automatic pre-processing phase, the synthetic velocimeters are cosine-tapered to reduce the effect of windowing, and then high-pass filtered with cut-off frequency at 0.5 Hz to avoid amplification of noise at low frequency during the integration. We integrate the recordings to obtain displacement. Then we cut a window for S wave at the theoretical S wave arrival time considering a homogenous medium with S velocity equal to 3.1 km/s. We execute a cosine-tapering to reduce the effects of the S wave windowing.

We filter in pass-band to select the frequency range of investigation. As visible in the spectrum of the displacement (Figure 2.2.1.(e-f)),  $f_c$  is around 0.3 Hz, so the frequency ranges investigated are 0.15 – 0.5 Hz and 0.5 – 2 Hz, in order to explore contributions to the slip imaging around the corner frequency and at higher frequencies, respectively. In this latter frequency band, the slip amplitude is expected to decrease as  $k^{-2}$ , in the wavenumber domain.

A crucial element for back-projection is the choice of time window  $t_w$  to be applied for the stacking. A parametric investigation showed that the optimal choice of  $t_w$  is the reciprocal of the central frequency of the corresponding band that is, in our case, 3 s for the low frequency band and 0.7 s for high frequency band. To smooth the slip rate and slip time evolution we imposed a time window overlap of 0.5  $t_w$ .

The signals were back-projected on a fault plane centred on the hypocentre (Latitude=42.832°, Longitude=13.111° Depth=9.52 km) and having the prescribed focal mechanism (strike=151°, dip =56°, slip=-95°) and a rectangular shape with dimensions  $\sim 2L \times 2W$  (see section 2.2). Through a grid refinement analysis, we verified a consistency of the slip imaging for cell sizes ranging from 1x1 to 4x4 km. The presented results refer to the 1x1 km discretization.

## 4 Algorithms

---

Our goal is to explore two different approaches to get complementary images of the earthquake source at low frequencies (SLIPNEAR) and relatively high frequencies (BP). Each of these approaches is suitable for a given frequency range and is expected to provide reliable estimates of a given set of parameters.

In the following sections, we summarize the characteristics of each algorithm and provide the relevant references.

### 4.1 SLIPNEAR

---

SLIPNEAR is a method to obtain the slip distribution of earthquakes in near real time, which has been developed (CNRS partner) in the frame of the project and first tested on a list of large past earthquakes (Aquila 2009 (Mw 6.3), Norcia 2015 (Mw 6.5), Tohoku 2011 (Mw 9.1), Lefkada 2015 (Mw 6.5), Illapel 2015 (Mw 8.3)). It is based on the inversion of regional seismograms, either broadband or strong motion. We qualify the method as “near real-time” since SLIPNEAR does not work directly on the real

time data flows but it is triggered once a hypocenter and a focal mechanism have been determined via an independent approach. When these are available, the required N, E, Z seismic traces are extracted from the database.

The objective of SLIPNEAR is to estimate the basic, though important, properties of the rupture, such as the extension of rupture along strike and dip, the location and value of maximum slip, and the relative location of slip with respect to the hypocenter defining the directivity effect. This in a relatively short time span (< 1 hour). In addition, by testing the two nodal planes of focal mechanisms, we expect that the actual rupture plane may be identified, at least in favorable cases. On the other hand, we acknowledge that the rather coarse discretization of the rupture which is used may not permit resolving the precise shape of individual slip patches. Nor will it account for structural complexities, multi-fault ruptures, that may be involved in some earthquakes.

The method starts once a hypocenter, a magnitude, and a focal mechanism have been determined. The epicenter and the focal mechanism are held fixed. The initial value of the magnitude is used to scale parameters of the rupture model. The hypocentral depth will be re-evaluated to some limited extent and the moment magnitude (seismic moment) will be re-determined.

Since the initial depth provided by the agencies that locate earthquakes in near real-time may not be determined with a high degree of accuracy, we systematically test three different hypocentral depths. Tested values are: 5, 8, 12 km if initial depth is smaller or equal to 10 km, and tested values are initial depth multiplied by a factor 0.7, 1.0, and 1.3 for greater initial depth.

#### 4.1.1 Kinematic models and inversion

The final result of SLIPNEAR corresponds to a 2D rectangular kinematic source model for each nodal plane of the focal mechanism. However, a first stage of inversion is carried out with a simple linear (1D) source model, for two purposes: i) to run a first and fast inversion allowing to identify seismic stations or individual components that may have trouble to be fitted and which will be discarded in the 2D inversion. This point is particularly important for near real time automated implementation in which the records will not be checked by the user; and ii) to identify the lateral extension of rupture along strike, allowing to limit the surface area of the 2D rectangular model.

The overall inversion is performed in four sequential stages, launched simultaneously for both nodal planes of the focal mechanism and for three different hypocentral depths. We list below the different stages which are illustrated on Figure 3.1.1.

**STAGE 1:** 1D linear source inversion.

**STAGE 2:** 2D rectangular source inversions for three different relative positions of the hypocenter on the rupture plane.

**STAGE 3:** four additional 2D rectangular source inversions using the best relative position of the hypocenter found in stage 2, but with different initial conditions or station weightings.

**STAGE 4:** computation of an average model from five 2D rectangular source inversions (the best of stage 2 plus the four of stage 3), and perform simple statistics to assess the robustness of the result and determine if the actual fault plane can be discriminated.

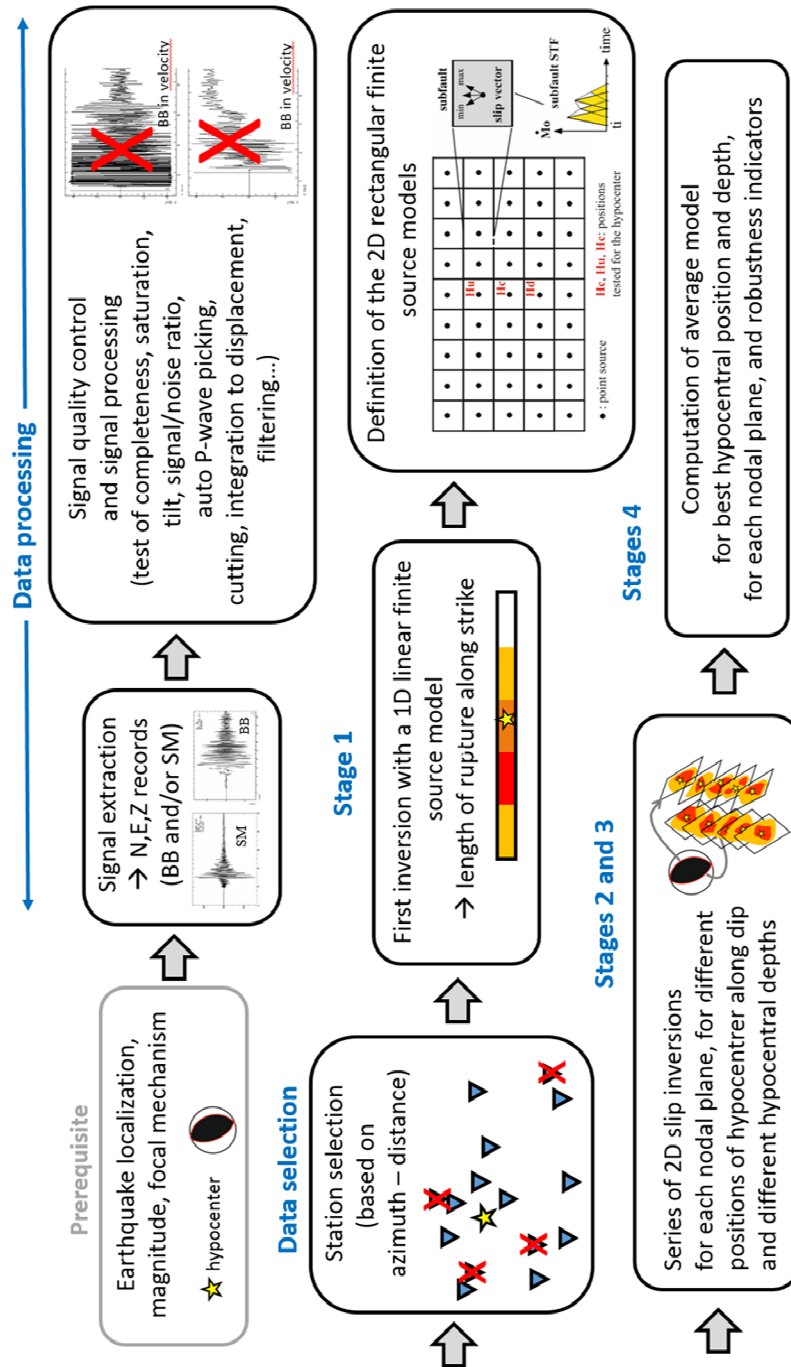


Figure 3.1.1: Illustration of the different steps in the SLIPNEAR method. BB: broadband records; SM: strong-motion records;  $M_0$  with a dot above means seismic moment rate;  $t_i$  is the rupture initiation (onset) time of a given subfault.

Regarding the 2D rectangular model, length along strike is scaled with the initial magnitude. It is taken large enough to account for possible unilateral ruptures in the strike or in the anti-strike direction. For example, model length is of the order of 70 km for  $M=6.5$ , 230 km for  $M=7$ , and 1800 km (i.e. 900 km on both sides of the hypocenter) for  $M=9$ . The ratio between width and length of the 2D model varies as a function of magnitude, from 1 (squared fault) for  $M < 6.5$ , to 0.3 (elongated fault) for  $M > 8.5$ . If model width, taking into consideration fault dip and hypocenter depth, implies that the model goes to the air, width is reduced so that the top of the model is fixed to the surface. The number of points

sources, representing subfaults, used to discretize the rupture along strike varies with the magnitude, from 9 for  $M < 6.5$  to 21 for  $M > 9$ .

Rupture along dip is discretized into five rows of point sources (subfaults). We initially tested models subdivided into three rows only, hence having even less parameters, but they provided poor representations of earthquakes whose slip is dominantly distributed along dip. This limited number of rows, five, is retained as a best compromise considering two imperatives: resolving the main characteristics of slip distributions that may take a wealth of different shapes, and limiting the number of parameters to be inverted for.

A local moment rate source time function is associated with each point source (subfault), discretized by a series of four mutually overlapping isosceles triangles (Figure S1). The onset time of each point source, the rake angle, and the amplitudes of the triangular elements (Figure S1) are inverted for using a simulated annealing algorithm. Rupture onset times of the subfaults (point sources) are bracketed using two bounding rupture velocities, 1.0 and 3.5 km/s. The slip angle (rake) may vary by  $\pm 45^\circ$  around the value corresponding to the focal mechanism. The criterion to assess the quality of the solution is the minimization of the normalized root mean square (RMS) misfit error on the waveforms, with a constraint to minimize the total seismic moment. This additional constraint helps avoiding spurious slip in parts of the model which are not constrained by the data. Synthetic seismograms are computed using the discrete wavenumber method of Bouchon (1981) designed for 1D velocity models.

In STAGE 2, we test three different positions of the hypocenter on the rupture plane: one is at the center (Hc), and the other two are one row up (Hu) and one row down (Hd) (Figure S1). The two latter are included to better represent possible up-dip or down-dip ruptures. This means that for a given hypocentral depth, three different slip inversions, corresponding to the three alternative position of the hypocenter on the rectangular model, will be performed for each nodal plane. In these three inversions, the relative position of the model with respect to the hypocenter is varied but the absolute position (lat, long, depth) of the hypocenter is kept fixed. In other words, the model is shifted updip or downdip of the hypocenter.

In STAGE 3, the relative position of the hypocenter (Hc, Hu, or Hd) providing the lowest RMS misfit value is retained, and four additional slip inversions are carried out with this position. In these four new inversions, we modify several conditions that will affect the inversion result: change the seed used to initiate the generator of random numbers in the simulated annealing scheme; change the initial values of the inverted parameters; change the parameters controlling the convergence of the simulated annealing; change the order in which subfaults are explored; change the weight of individual stations in the dataset by  $\pm 30\%$  (maintaining equal the sum of weights).

## Average slip model

From the five individual slip models resulting from the inversions with the best relative position of the hypocenter (that of STAGE 2 and the four of STAGE 3), we calculate an average model by computing the mean values of the inverted parameters at each point source, weighted by the inverse of the RMS misfit value of the corresponding model. We obtain an average distribution of slip in amplitude and rake.

## Model discrepancy

Although our final model is the average one, we keep track of the five individual slip models to assess the stability of the solution. For that purpose, we developed a measure of the discrepancy between slip models, called model discrepancy (MD). In the computation of MD, we do not compare simply the slip values of individual subfaults occupying exactly the same position on different models, but we compare

values of slip averaged per area. This indicator is needed to assess to which extent the different models found for each nodal planes are similar (low MD) or distinct (high MD).

## Index of confidence on the stability of the slip map

All what is described in this paragraph is done independently for each nodal plane. First of all, we select as final result the average slip model corresponding to the depth associated with the lowest RMS waveform misfit. Then, we build an index of confidence measuring the stability of the slip distribution based on the following indicators: (1) the value of model discrepancy (MD) calculated over the five individual slip models for the best depth; (2) the quality of the waveform fit (RMS misfit function); (3) the number of components (records) finally retained in the inversion; (4) the variability of peak slip; and (5) the variability of moment magnitude. The index of confidence increases for lower values of MD, lower values of RMS misfit, higher number of components, and smaller variability in maximum slip and in Mw. The index may vary between 0 and 100%, 0 meaning unconstrained, not reliable, result, and 100% highly constrained and reliable slip map. Each nodal plane ends up with its own index of confidence on the stability of its slip map.

## Index of confidence on the discrimination of the rupture plane

We build an index of confidence measuring to which extent the results from one nodal plane are systematically better than those of the other plane. The index is based on the following indicators: (1) the differences in RMS misfit functions obtained for the two nodal planes; (2) the number of times over the 15 inversions carried out for each plane (3 depths x 5 inversions) that each plane resulted in a lower RMS misfit than the other; and (3) the number of components retained in the inversion for each plane. The index of confidence on the discrimination increases if one of the nodal plane provided lower rms misfit values for a majority of inversions and if it permitted the modelling of more components. The index may vary between 0 and 100%, 0 meaning no discrimination at all and 100% strong discrimination.

## 4.2 Back-Projection

---

Within this Task, UNINA's team has been working at the development of a dedicated platform (in Matlab environment) that develops a beamforming and stacking technique to back-project the direct P or S-wave recorded amplitudes into the source region, following the approach of Maercklin *et al*, 2012. The slip imaging approach combines a spatial weighted estimate on where seismic energy is radiated with proper scaling of the recorded displacement amplitudes to recover the slip rate amplitude at the source as a function of space and time.

Specifically, the procedure is structured as follows:

- The earthquake source region is subdivided into a grid of small sub-sources, and for any given sub-source the delay times are computed to all seismic stations relative to a reference station.
- The recorded amplitudes at all stations, within a time window bracketing the theoretical times, are summed using a weighted stacking to enhance coherent arrivals, and the obtained coherency value is assigned to the current sub-source. The time window for a single back-projection image is based on the period of the dominant phases. Repeating this process for all sub-sources provides the back-projected coherency distribution in the earthquake source region at a given arrival time.
- For computation of the slip rate, the displacement amplitudes appropriately corrected by distance  $R_{ij}$  (the geometrical spreading) and radiation pattern  $F_{ij}$  for a constant focal mechanism are stacked

and back-projected for all possible elementary sources located along the fault surface. The resulting slip rate for the  $i$ -th grid point and at the time  $t$  is obtained as the summation:

$$\dot{S}_i(t) = \frac{2\pi\rho v_s^3}{\mu AN_s} \sum_{j=1}^{N_s} \frac{R_{ij}}{F_{ij}} U_j(t + t_i^R + \delta t_{ij}) \quad (3.1)$$

where  $U_{ij}$  is the observed displacement at the  $j$ -th station,  $t_i^R$  the travel-time to the reference station,  $\delta t_{ij}$  the time shift between the  $j$ -th station and the reference station,  $N_s$  the number of station,  $\rho$  is the crustal density,  $v_s$  the S-wave velocity,  $\mu$  the shear modulus, and  $A$  the area of the sub-fault.

- We define an objective function for slip source location as the standard weighted back-projected stack amplitude for the  $i$ -th grid point and the time  $t$ :

$$W_i(t) = C(t) \left( \sum_{j=1}^{N_s} \text{sign}(U_j)^n \sqrt{|U_j(t + t_i^R + \delta t_{ij})|} \right)^n \quad (3.2)$$

where the normalization factor  $C(t)$  ensures that the sum of  $W$  over all grid points is 1, so that the  $W$  function will be used as a spatial weighting function, assigning a larger value to fault points where most likely high-radiating asperities were located.

- The final slip rate map is obtained as the product  $W_i \cdot S_i$ , while the integration over time provide the final slip imaging

## 5 Results

### 5.1 SLIPNEAR

---

#### Inversion of synthetic data

The synthetic data described in section 2.1.1 are used as input data for a SLIPNEAR inversion. The SLIPNEAR version used here is the same as for the automated near-real time implementation, except for two points: i) since synthetic signals do not incorporate the same kind of pre-event noise nor the high frequencies present in the real earthquake data, we cannot use the automatic picker of the P-wave. We had to manually pick the first P wave onsets; and ii) since the synthetic signals were computed down to 0.05 Hz, we introduced this lower limit in frequency in the SLIPNEAR code.

The hypocenter location and the focal mechanism (prerequisite) are those used to generate the input synthetic waveforms. On the other hand, the velocity model used to compute the waveforms in SLIPNEAR is a generic model used in the near real-time implementation which is different from the model used to generate the input synthetic waveforms.

The result is illustrated in Figure 4.4.1. The overall shape of the main slip zone is well retrieved. The maximum slip is slightly underestimated, but this may be related to the fact that the peak slip in the synthetic model (d) occurs in small scale areas and it is hence associated to smaller wavelength asperities, while the discretization of the rupture in the SLIPNEAR model (b and c) is much coarser (larger subfaults). The narrow slip zone is imaged along a single row of point sources, corresponding to

individual subfault areas of 7 km x 4.6 km, meaning that the seismic moment, and therefore slip, is averaged over relatively large areas. Waveforms fit is acceptable acknowledging that the velocity models used are different. This suggests that the inversion is slightly sensitive to the velocity model in the frequency range used by the SLIPNEAR inversion (here between 0.05 and 0.14 Hz).

The index of confidence on the slip map is 91%, meaning that the slip map is well constrained by data, as expected given the excellent azimuth – distance distribution of stations around the rupture area.

On the other hand, the index of confidence on the discrimination of the fault plane is low, 48%, meaning that the input waveforms can be modelled almost as well by the auxiliary plane dipping to the NE. We relate this undiscriminating behavior to the fact that the two nodal planes of the focal mechanism have the same azimuth, only differing into the dip direction, combined with a slip distribution elongated along strike without significant extension along dip. In other words, the discrimination of the actual rupture plane from the auxiliary plane in the case of dip-slip events may be possible only if the slip is distributed to a larger extent along the dip direction.

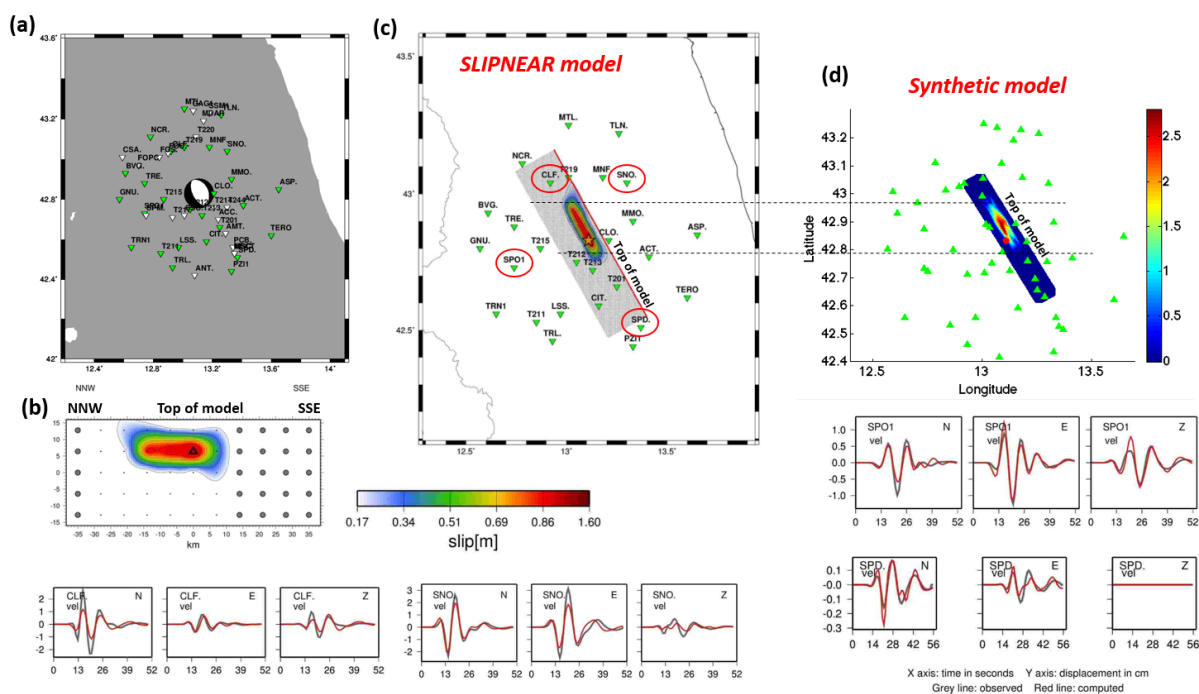


Figure 4.1.1. Result of the SLIPNEAR inversion of the synthetic dataset and comparison with the synthetic model. The rupture plane represented strikes N151 and dips  $56^\circ$  to the SW. (a) Map of stations for which synthetic seismograms were provided, with stations finally retained in the inversion in green (automatic selection based on the azimuth and distance distribution). Also shown the focal mechanism used (same as that of the synthetic model). (b) Slip map obtained by SLIPNEAR, shown in the strike – dip plane. Small dots show the position of point sources used to discretize the rupture model. Large grey dots are point sources which were discarded after the initial line source inversion. (c) Slip map from SLIPNEAR projected into the surface and used stations (green triangles). Red open ellipses mark the four stations whose waveform modeling is shown in the lower part of the Figure. To save space, we show the waveform fit for 4 stations only, one directive (CLF), one in the opposite direction (SPD), and two stations perpendicular to the fault, on each side (SNO and SPO1). (d) Synthetic slip model for comparison. Waveforms are in displacement (cm), grey for input synthetic data and red for waveforms computed with the SLIPNEAR model. The flat signals on the vertical (Z) component of station SPD means that this component was discarded during the inversion. ‘vel’ means that the original input synthetic records were in velocity.

## Inversion of real data from the 2016 Norcia earthquake (Mw 6.5)

The station distribution is similar to that of the synthetic case, corresponding to the strong motion records available from the “ESM - Engineering Strong-Motion database” (<https://esm.mi.ingv.it>) at distances less than 45 km. Given the density of the strong-motion network, it is not necessary to use stations at larger distances.

The focal mechanism is fixed to (strike, dip, rake) = (155, 47, -90), corresponding to the fault plane used by Scognamiglio et al. (2018) to model the main rupture plane of the 2016 Norcia earthquake. The velocity model used is a generic model used in the near real-time implementation. Waveforms are filtered in the frequency range 0.015 to 0.14 Hz (may be narrower for some components).

As shown in Figure 4.1.2, the slip map obtained by SLIPNEAR compares well with those published by Pizzi et al. (2017) and Scognamiglio et al. (2018). Pizzi et al. (2017) used strong-motion data only, while Scognamiglio et al. inverted jointly strong-motion and GPS data, and both published models are more finely discretized than the SLIPNEAR model. As in the case of the synthetic data inversion (previous section), SLIPNEAR maximum slip is lower than in finer models. However, SLIPNEAR retrieved the main characteristics of the Norcia earthquake, corresponding to a main slip patch of about 10 km extension located up-dip and to the SSE of the hypocenter, with maximum slip reaching 2 to 3 m. Nonetheless, we have to state that SLIPNEAR cannot resolve accurately slip at the surface, due to the coarse spatial discretization.

The index of confidence on the slip map is 100%, meaning that the slip map can be considered as well constrained by the data. Again, such a result is somewhat expected given the excellent azimuth – distance distribution of stations around the rupture area.

On the other hand, the index of confidence on the discrimination of the fault plane is low, 34%, meaning that the input waveforms can be modelled almost as well by the auxiliary plane dipping to the NE. This could be related to the dip-slip mechanism and the relatively narrow extent of the slip distribution along dip, as discussed in the synthetic case above. Discrimination may be also complicated by the fact that we do not take into account the second oblique rupture plane proposed by Scognamiglio et al. (2018), whose effect would be present in the recorded waveforms and not in the computed ones.

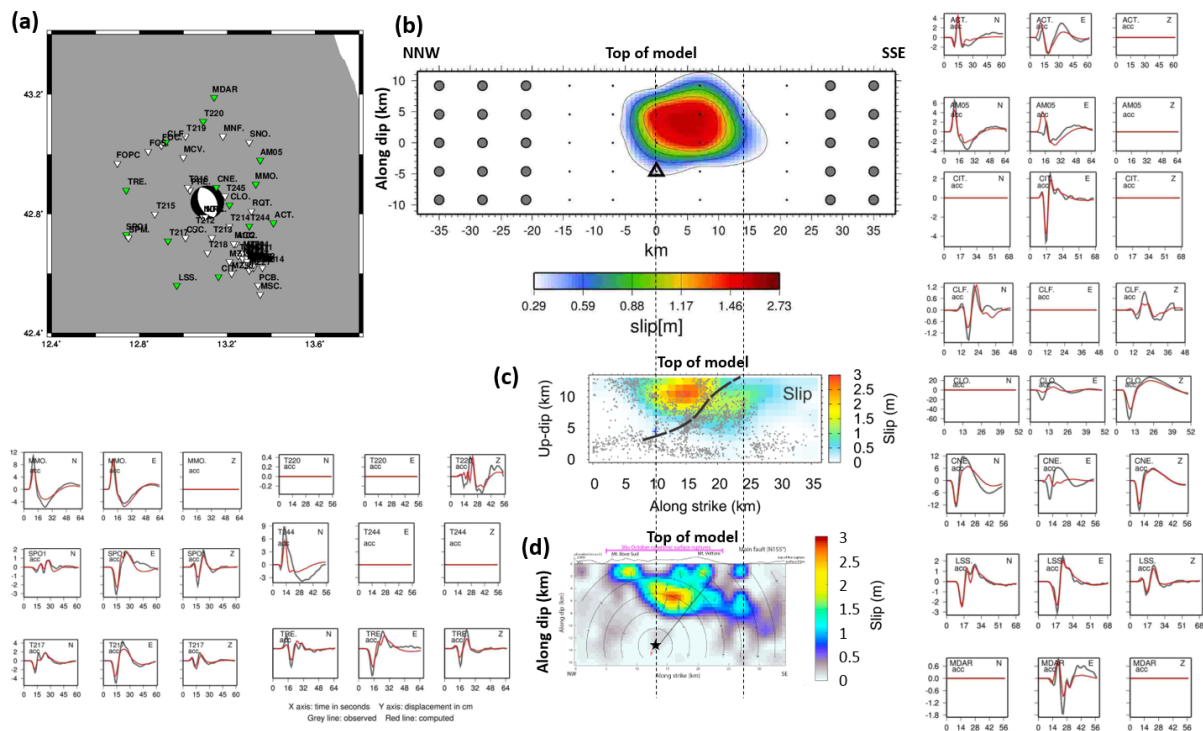


Figure 4.1.2. Result of the SLIPNEAR inversion of the real dataset from the 2016 Norcia earthquake (Mw 6.5) and comparison with published slip models. The rupture plane represented for SLIPNEAR strikes N155 and dips  $47^\circ$  to the SW. (a) Map of strong-motion stations, with stations finally retained in the inversion in green (automatic selection based on the azimuth and distance distribution). Also shown the focal mechanism used. (b) Slip map obtained by SLIPNEAR, shown in the strike – dip plane. Small dots show the position of point sources used to discretize the rupture model. Large grey dots are point sources which were discarded after the initial line source inversion. (c) Slip map obtained by Pizzi et al. (2017). (d) Slip map obtained by Scognamiglio et al. (2018) for the main fault plane. These authors included a second rupture plane, oblique with respect to the main one, not shown on the Figure. We also show the waveform fit in displacement (cm), grey for observed data and red for waveforms computed with the SLIPNEAR model. Flat signals mean that the corresponding components were discarded during the inversion. ‘acc’ means that the original records were in acceleration (strong-motion instruments).

## Results from the SLIPNEAR implementation in near real-time

The SLIPNEAR method has been implemented to work in a fully automated way in near-real time. A script running permanently in the background is scanning every 5 minutes the events list of the USGS and the EMSC. Once a new event has been detected with a magnitude larger or equal to 5.8 anywhere in the world, the regional seismological records are retrieved via *fdsn* webservice and a waveform inversion is launched to determine the focal mechanism with the FMNEAR approach (Delouis, 2014). If the focal mechanism obtained is well constrained by the data, the SLIPNEAR inversion is launched, testing the two nodal planes of the FMNEAR mechanism.

Publication of the SLIPNEAR result is not yet automated. If the indicators of the solution are good enough, the result is published “manually” on the twitter social media, with a delay depending on the availability of the author (B. Delouis).

## The 2019/07/06 M7.1 Ridgecrest (California) earthquake

The SLIPNEAR result was the first finite fault model published for this earthquake, before the USGS one. The NW-SE (strike 320°) rupture plane was correctly identified by SLIPNEAR as the rupture plane, as confirmed latter on by surface ruptures, aftershocks, InSAR, and optical image correlation. Indexes of confidence on the discrimination of the rupture plane and on the slip map are 100% and 100% respectively. These high (maximum) values of the indexes of confidence are likely related to the quality of the seismic network in the rupture area, which is dense and comprises many strong-motion instruments. The focal mechanism being of strike-slip type with the two nodal planes extending in perpendicular directions, discrimination of the rupture plane is facilitated (Figure 4.1.3).

Link to the twitter publication, showing the focal mechanism used, slip map, waveform modelling, and more details on the solution:

<https://twitter.com/BertrandDelouis/status/1147390784112644096>

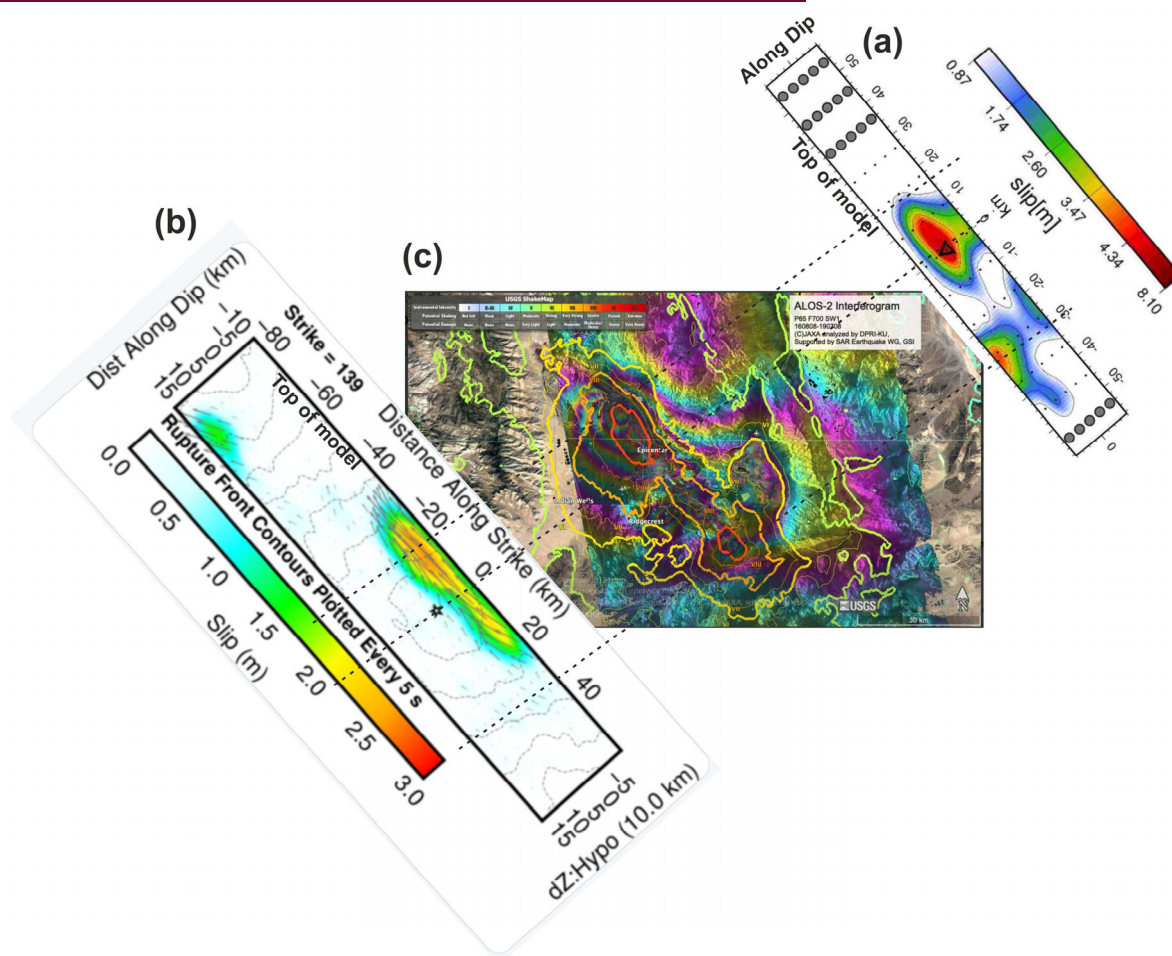


Figure 4.1.3: Comparison between SLIPNEAR result (a), USGS finite fault model (b) ([https://twitter.com/gph\\_seismo/status/1147395573420580864](https://twitter.com/gph_seismo/status/1147395573420580864)) and (<https://earthquake.usgs.gov/earthquakes/eventpage/ci38457511/executive>), and the ALOS InSAR interferogram with superimposed intensity map from USGS (c, <https://twitter.com/manabu0131dpri/status/1148579935142809600>) for the Ridgecrest earthquake. Note the good correlation between the SLIPNEAR slip patches and the intensity map. All slip maps represented in the strike - dip plane.

## The 2019/07/04 M6.4 Searles Valley (California) earthquake

The SLIPNEAR result was the first slip map published for this earthquake, and the USGS did not publish any finite fault model for that event. The NE-SW (strike 45°) rupture plane was correctly identified by SLIPNEAR as the rupture plane, as confirmed latter on by surface ruptures, aftershocks, InSAR and optical image correlation. Indexes of confidence on the discrimination of the rupture plane and on the slip map are 100% and 95% respectively. These high (maximum) values of the indexes of confidence are likely related to the quality of the seismic network in the rupture area, which is dense and comprises many strong-motion instruments. The focal mechanism being of strike-slip type with the two nodal planes extending in perpendicular directions, discrimination of the rupture plane is facilitated.

Link to the twitter publication, showing the focal mechanism used, the slip map, the waveform modelling, and more details on the solution:  
<https://twitter.com/BertrandDelouis/status/1147113233121234944>

## The 2018/09/28 M7.5 Palu (Indonesia) earthquake

It is not clearly established whose slip map was published first, among SLIPNEAR and the USGS, but the first finite fault model published by USGS proved to be clearly incompatible with subsequent information. First USGS finite fault model exhibited a main slip patch located north of the epicenter whereas subsequent InSAR, optical image correlation, and aftershocks data showed that the rupture propagated towards the South. The SLIPNEAR model was published when interpretations of satellite data were not yet available, and it shows a clear dominant unilateral rupture towards the South. The NS rupture plane is identified with a confidence index of 100% and the index of confidence on the slip map is 71%. The USGS updated much later, on October 17, 2019, its finite fault model (Figure S5c), with a main slip patch south of the epicenter (see Figure 4.1.4).

Link to the twitter publication, showing the focal mechanism used, the slip map, the waveform modelling, and more details on the solution:  
<https://twitter.com/BertrandDelouis/status/1045945940723617793>

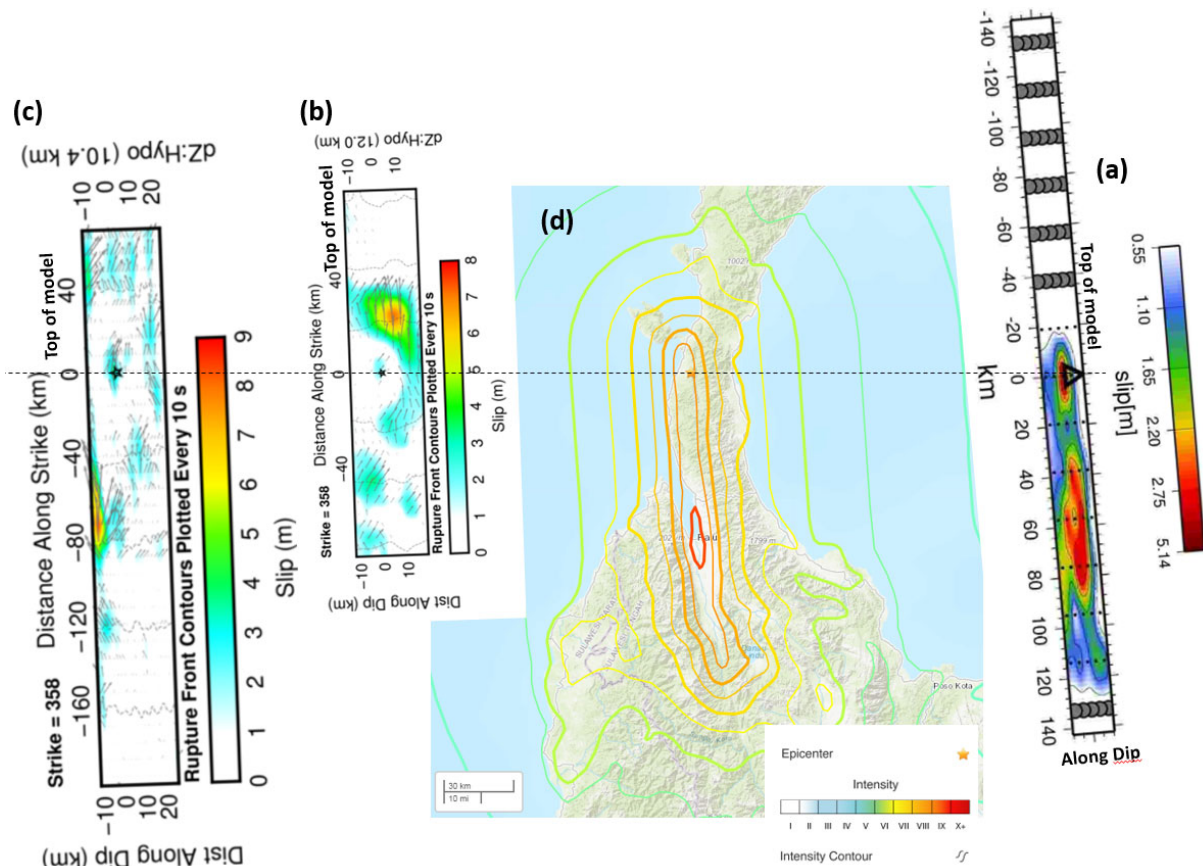


Figure 4.1.4: Comparison between SLIPNEAR solution (a), USGS finite fault models (b and c), and the intensity map from USGS (d, <https://earthquake.usgs.gov/earthquakes/eventpage/us1000h3p4/executive>) for the Palu earthquake. USGS slip map (b) was produced in the hours following the earthquake. Slip map (c) is the updated version by the USGS more than two weeks later. SLIPNEAR result (a) published in the hours following the earthquake clearly shows the unilateral propagation towards the South, and correlates well with the USGS intensity map. All slip maps represented in the strike - dip plane.

## The 2018/10/28 M6.8 Ionian Sea (Greece) earthquake

The SLIPNEAR result was the only finite fault model published in the hours and days following the earthquake (no model from the USGS). The NS, east-dipping plane, of the focal mechanism was identified by SLIPNEAR as the rupture plane. Index of confidence on the discrimination of the rupture plane and on the slip map are 100% and 85% respectively (See figure 4.1.5).

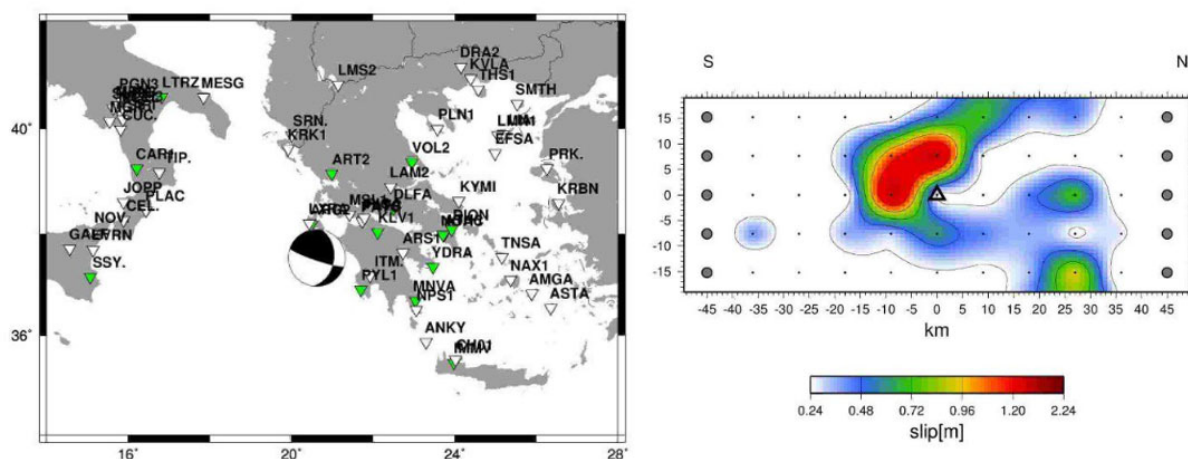


Figure 4.1.5. SLIPNEAR result for the Ionian Sea earthquake. Map of the stations used (left) and slip map obtained for the selected rupture plane striking NS and dipping to the East (right). The main slip patch is located south of the hypocenter (triangle). Slip map represented in the strike – dip plane.

Link to the twitter publication, showing the focal mechanism used, the slip map, the waveform modelling, and more details on the solution: <https://twitter.com/BertrandDelouis/status/1055713092372434944>

The selection of the NS striking and east-dipping plane as the rupture plane, and the directivity towards the South, were confirmed by Papadopoulos et al. (Abstract EGU Vienna April 2019) <https://meetingorganizer.copernicus.org/EGU2019/EGU2019-13705.pdf>

## 5.2 Back-Projection

As shown in equation 3.1, the algorithm computes the slip rate for each cell  $i$  as the average of the recorded displacements at the stations  $j$ , normalized to the distance  $R_{ij}$  and corrected for the radiation pattern  $F_{ij}$ . For stations close to the nodal plane of a sub-source, or when there is a change of polarity in the radiation pattern for the SV component, the radiation pattern is close to zero and this may generate instability in the final solution.

To prevent this instability, for some applications, a constant average radiation pattern can be applied. This is the case, for example, of regional back-projection applications, with all the stations on the same side with respect to the fault (Maercklin et al., 2012)

In principle, to back-project near-source data distributed all around the fault, we cannot neglect the variability of the radiation pattern. Therefore, we define a threshold level  $I_w$ , such that the effective  $F_{ij}$  used in equation 3.1 is imposed to be equal to  $I_w$  when  $F_{ij} < I_w$ .

We choose the threshold level  $I_w$  equal to 0.05 that is  $\sim 10\%$  of the average radiation pattern for the SV decomposition of the S-wave phase. We verified the adequacy of this choice, by investigating the maximum slip as a function of the imposed threshold and evidencing how the solutions become unstable for a threshold smaller than 0.01.

We considered all the stations within the range of distances 15-45 km (Figure 4.2.1a) to minimize near-field effects and avoid a lack of resolution due to an excessive attenuation for distant stations. In figure

4.2.1(b) the vertical displacement at the stations is shown, after the cut for S arrival time and the filtering in the low frequency range (0.15-0.5) Hz. In figure 4.2.1(c) the displacements at the stations, after the time shift with respect to the reference station, are represented. The closest station to the hypocentre is chosen as reference station.

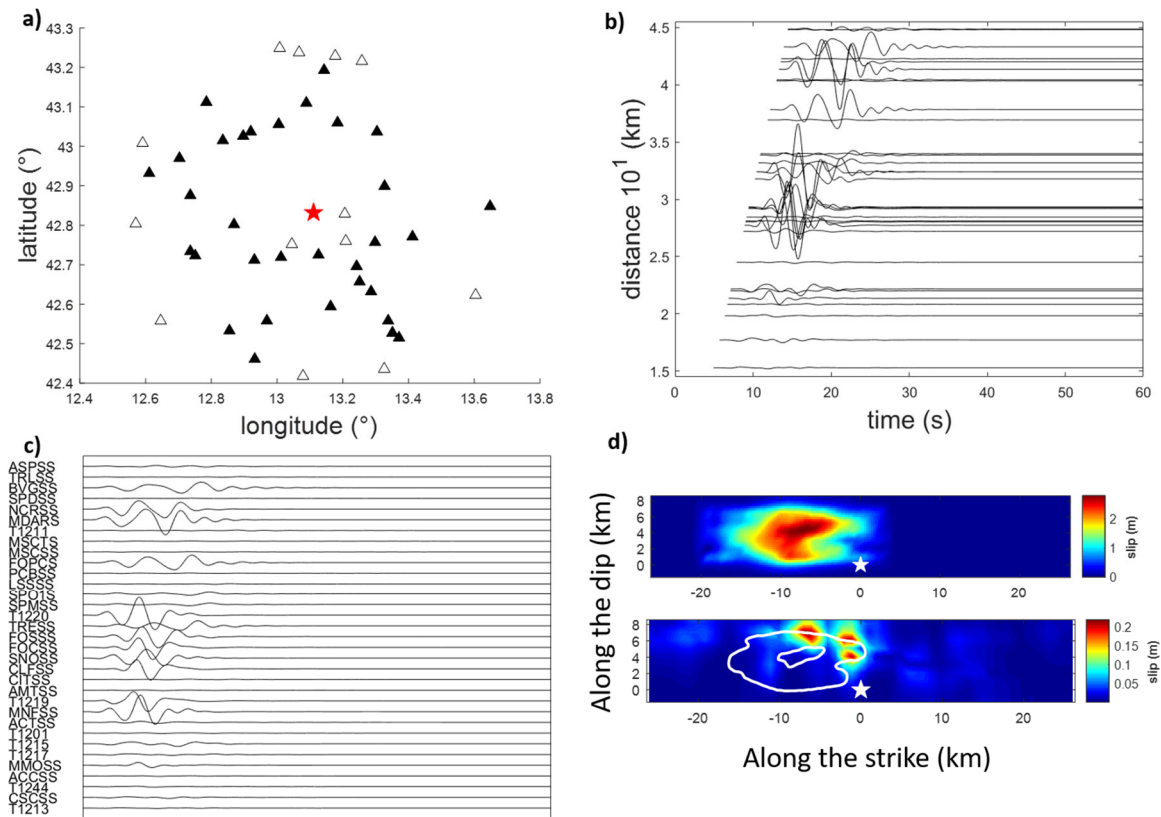


Figure 4.2.1 Results of back-projection back-projecting the data from all the stations within the range [15-45 km] and in the frequency band [0.15-0.50Hz] : a) Map: epicenter is represented as a red star, stations are represented as triangles, black triangles are stations within (15-45) km, white triangles are outside of this range; b) displacement windows for stations ordered in growing distance; c) windows ready for the stacking after time shift respect the reference station, ordered in growing distance (as in b) with corresponding stations names; d) on top the true slip map, on the bottom interpolated slip map found by back-projection, for both top and bottom the white star represents the hypocenter and colors are for the values of slip (m). The white lines in the bottom are level curves of true model for 1 and 2.5 m of slip respectively.

In figure 4.2.1(d – bottom panel), the final back-projected slip is plotted along with the 1 m and 2.5 m isolines of the true model (top panel of figure 4.2.1(d)). We represent the up-dip results, which is the only part interested by dislocation, while in the down part of the fault we do not find any significant dislocation. Considering the true model  $k^{-2}$  slip distribution, these isolines can be considered as a good proxy of the boundaries of the maximum slip patches for the long ( $k < k_c$ ) and short ( $k > k_c$ ) wavelength respectively (Figure 2.2.1 (a)). In this framework  $k_c$  is the corner wavenumber beyond which the slip spectral amplitude is expected to decay as  $k^{-2}$ . The position of the main patch of slip correctly reproduces the NNW directivity of the true model with the highest slip values are located on the borders of the 1 m isoline. However, the final slip values are about one order of magnitude smaller with respect to the final slip of true model. In figure 4.3.2, slip rate snapshots referred at rupture time show the rupture propagation vs time toward SSE respect the hypocentre, while in the true model the rupture propagates toward NNW.

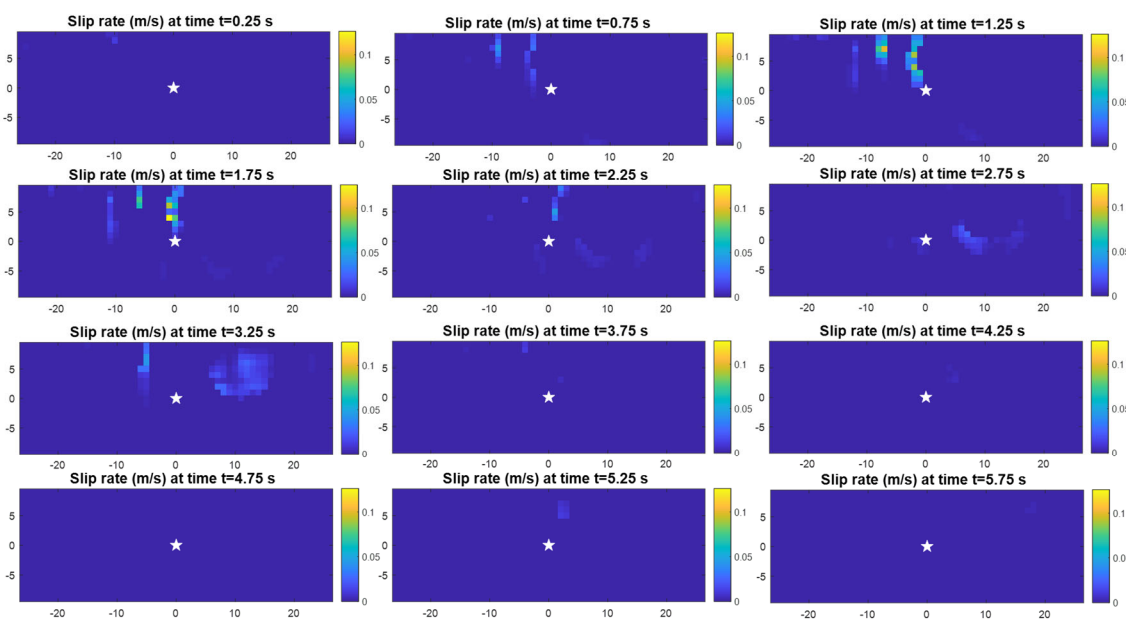


Figure 4.2.2 Slip rate stations within [15-45] km and in (0.15-0.5) Hz for growing time referred at rupture time. The white star represents the hypocentre, the colors represent the slip rate (m/s).

The same analysis, using the same station configuration (Figure 4.2.2(a)), has been carried out for the high frequency range [0.5-2 Hz]. As previously, in the Figures 4.2.2(b) and (c) we plot the vertical displacement filtered and shifted, respectively. Differently from the previous case, the main patch of slip is now located on the 2.5 m isoline (Figure 4.2.2(d)). In other words, as expected, the inversion in the low frequency band seems to locate the boundary of the longer wavelength slip patch. Conversely, the high frequency maximum slip is retrieved at the boundary of the short wavelength maximum slip. In both cases, the directivity is correctly modelled and the maximum slip is less than 10% as compared to the true model.

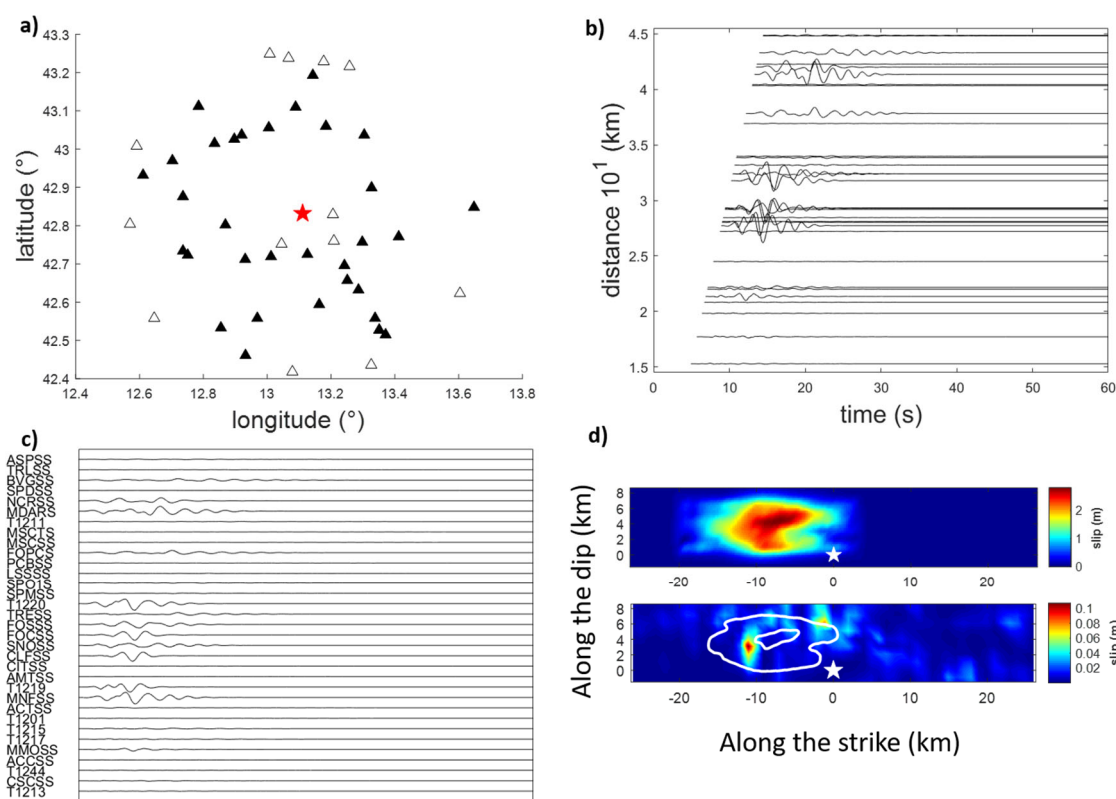


Figure 4.2.3 Results of back-projection back-projecting the data from all the stations within the range [15-45 km] and in the frequency band [0.5-2.0Hz] a) Map: epicenter is represented as a red star, stations are represented as triangles, black triangles are stations within (15-45) km , white triangles are outside of this range; b) displacement windows for stations ordered in growing distance; c) windows ready for the stacking after time shift respect the reference station, ordered in growing distance (as in b) with corresponding stations names; d) on top the true slip map, on the bottom interpolated slip map found by back-projection, for both top and bottom the white star represents the hypocenter and colors are for the values of slip (m). The white lines in the bottom are level curves of true model for 1 and 2.5 m of slip respectively.

When using all stations within [15,45] km, we found that the slip is well located, but suffers from an underestimation of amplitude as well as in reconstructing the rupture on the fault.

Back-projection generally is used in sub-networks and teleismic arrays, as in Satriano et al. (2014) and in Maerklin et al. (2012). This technique manages to focus the source contributions through the coherence of the waveforms. Therefore, the use of stations in opposite directions (for example directives and anti-directives) in near source and with a complete azimuthal coverage leads to solutions that are not reliable, since the signals can lose coherency and appear heterogeneous, without a clear common pattern. If we focus on small arrays of neighbour stations, on the other hand, since the stations are nearby, the waves travel through similar rays. In this study case, stations in the North side of the hypocentre (black triangles in figure 4.3.4(a)) the traces show more coherency and waveforms are very similar to each other's (figure 4.3.4(c)). Following this idea, we investigated the solutions for NNW group.

The results of the inversion using stations in the North side of the hypocentre, for a lower frequency band are shown in figure 4.3.4(d). The slip imaging shows values of higher slip with respect to the case

of considering all stations, with a maximum of the slip to the west of the hypocentre along the up-dip direction, in correspondence of the main patch of true model.

In figure 4.3.5, snapshots of the slip rate at different rupture times show the rupture propagation vs time toward NNW respect the hypocentre. At 4 s there is the maximum of slip rate relative to the main patch, while at 5.5 s we observe high value of slip rate at border, caused by the fact that the isochrones break off at the edge. At 9 s the rupture propagation is almost completely finished.

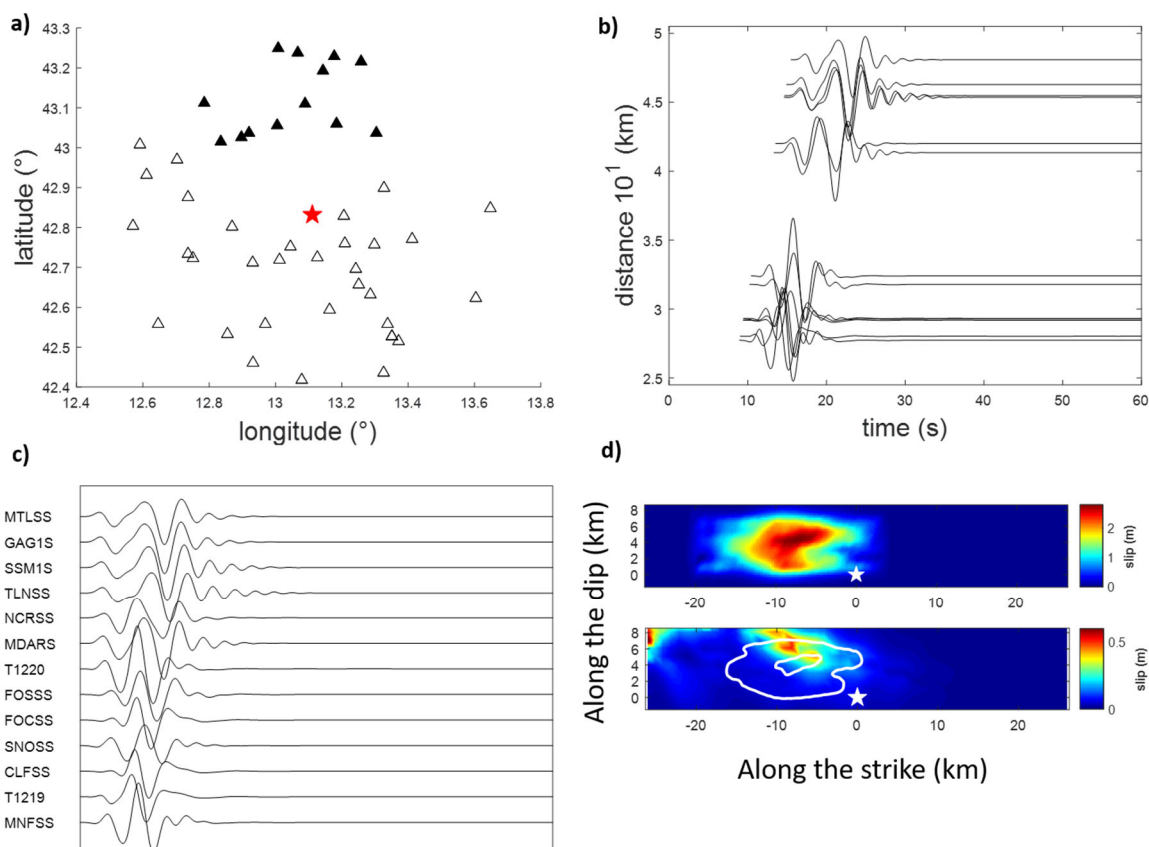


Figure 4.2.4 Results of back-projection back-projecting the data from North stations in the frequency band [0.15-0.5Hz] a) Map: epicenter is represented as a red star, stations are represented as triangles, black triangles are stations in the North side of the hypocenter, white triangles are outside this selection; b) displacement windows for stations ordered in growing distance; c) windows ready for the stacking after time shift respect the reference station, ordered in growing distance (as in b) with corresponding stations names; d) on top the true slip map, on the bottom interpolated slip map found by back-projection, for both top and bottom the white star represents the hypocenter and colors are for the values of slip (m). The white lines in the bottom are level curves of true model for 1 and 2.5 m of slip respectively.

For the higher frequency band, the final back-projected slip is plotted along with the 0.25 m and 0.5 m isolines of the high frequency  $k^{-2}$  contribution of true model (figure 4.3.6(d)). We found two maxima of final slip, one west of the hypocentre along the up-dip direction, located in the point of maximum  $k^{-2}$  contribution of true model, the other in the NNW direction about 20 km from the hypocentre along the direction of the strike, highlighting the border of the dislocation zone of the true model, although some spurious contributions appear on the boundary of the fault in the direction of the array.

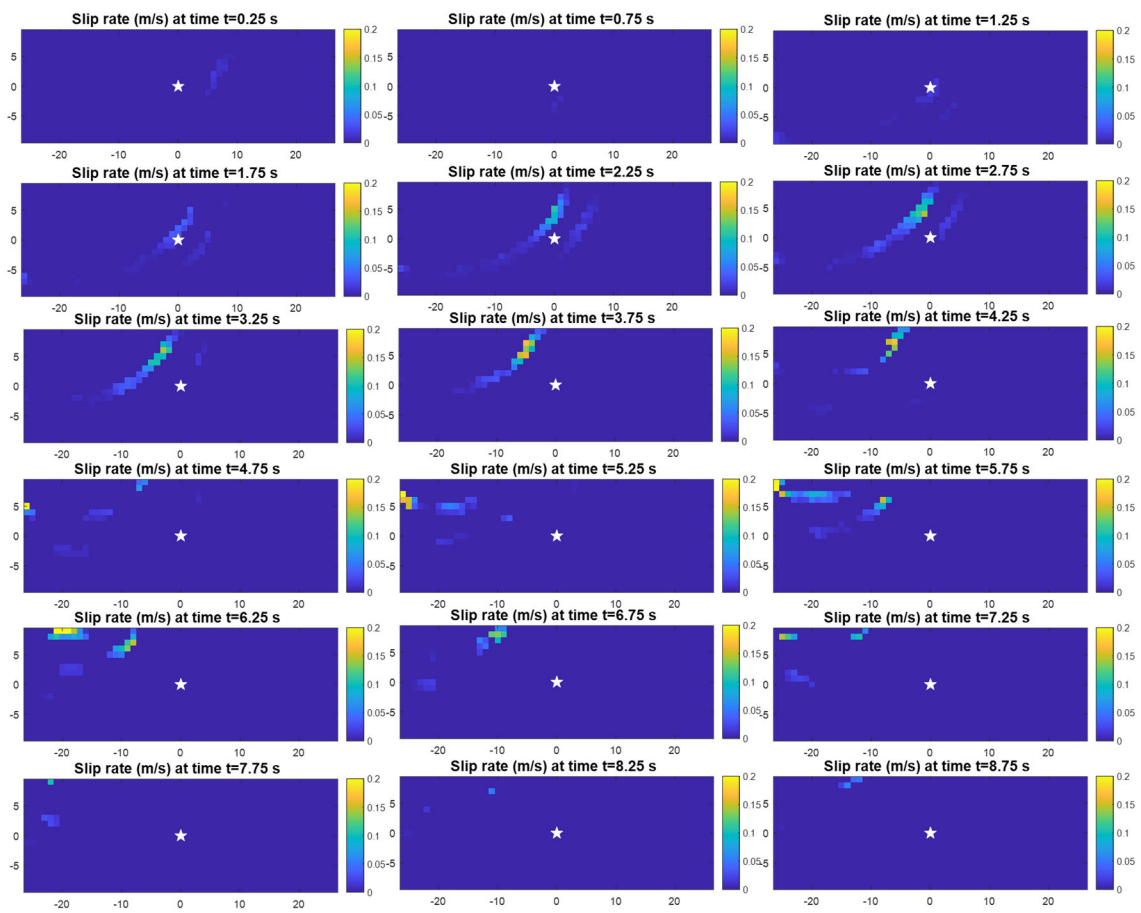


Figure 4.3.5 Slip rate for North stations in (0.15-0.5) Hz for growing time referred at rupture time. The white star represents the hypocentre, the colors represent the slip rate (m/s).

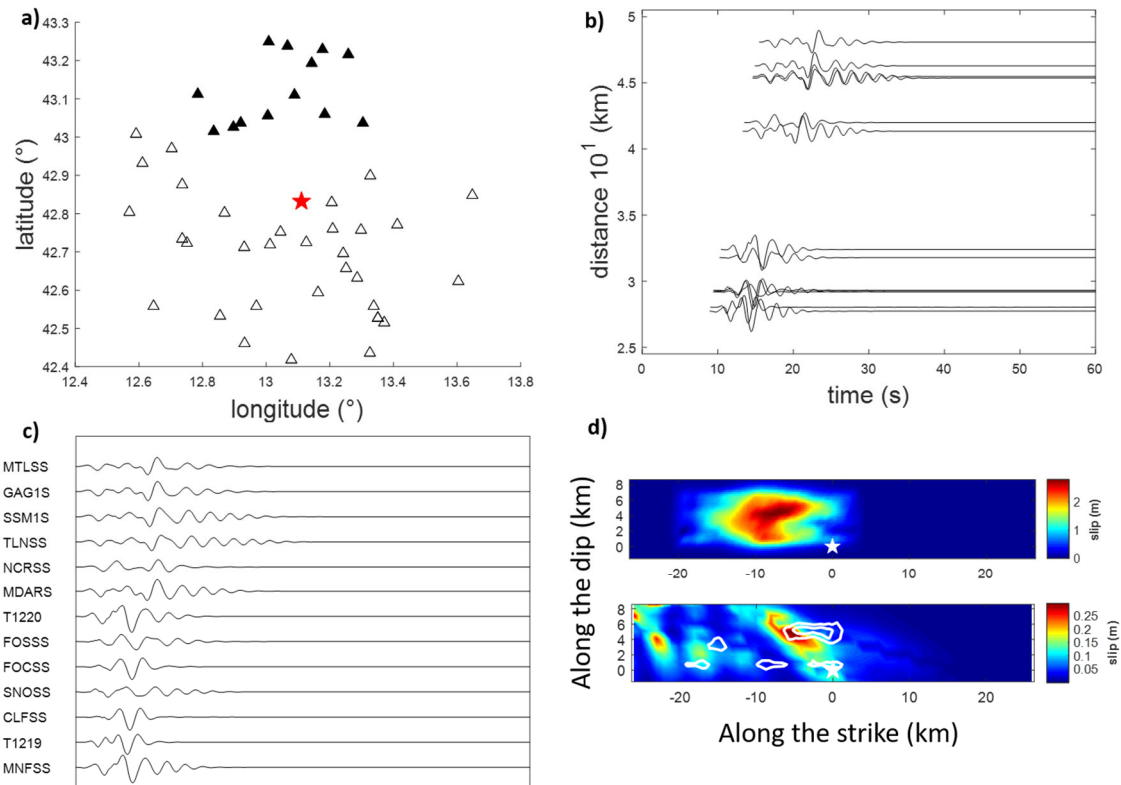


Figure 4.3.6 Results of back-projection back-projecting the data from North stations in the frequency band [0.5-2Hz] a) Map: epicenter is represented as a red star, stations are represented as triangles, black triangles are stations in the North side of the hypocenter, white triangles are outside this selection; b) displacement windows for stations ordered in growing distance; c) windows ready for the stacking after time shift respect the reference station, ordered in growing distance (as in b) with corresponding stations names; d) on top the true slip map, on the bottom interpolated slip map found by back-projection, for both top and bottom the white star represents the hypocenter and colors are for the values of slip (m). The white lines in the bottom are level curves of  $k^{-2}$  contribution of true model for 0.25 and 0.5 m of slip respectively.

## 5.3 Final remarks about back projection method

Back-projection is an effective method for imaging the major asperities of slip, in particular at high frequency, and allows modelling the areas in correspondence with the maximum slip and the stopping phase.

Another important result of back-projection is the indirect determination of the rupture velocity. For stations in the North direction, in the low frequency band (0.15-0.5 Hz), we consider the sub-sources that dislocated at least 10% of the maximum slip and picked the activation time of each sub-source as represented in figure 4.3.7(a) in colour on the fault plane, while the black contour are level curves for the activation time. The white line joins the points on the plane to which correspond the maximum slip rate over time. We represent the distance of the point at which occurs the maximum of slip rate in that time in Figure 4.3.7(b). An almost linear trend of the points suggests that the rupture velocity is uniform.

We estimate the average trend of the velocity rupture on the fault for time minor or equal to 6 s, since after that, as visible in the snapshot of the slip rate (figure 4.3.5), the rupture does not interest anymore the main patch, but border effects start in the shallow part. We obtain a velocity of  $2.4 \pm 0.3$  km/s (red line in figure 4.3.7(b)), while the velocity rupture for the true model is 2.72 km/s.

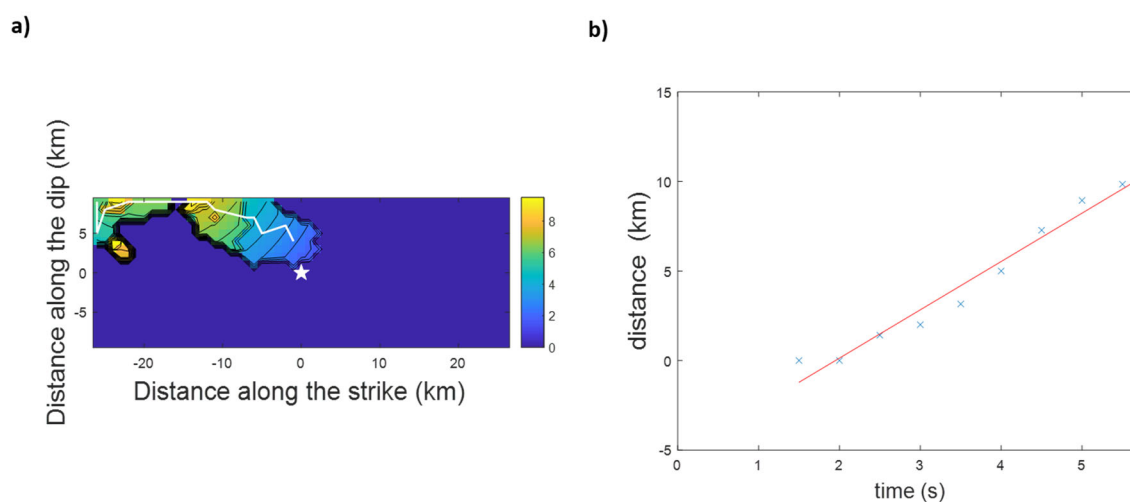


Figure 4.3.7 Velocity rupture: a) activation times in color on the fault of the sub-sources that have dislocated, the white star represents the hypocenter, the white line joins the points on the plane to which correspond the maximum slip rate over time; b) distance vs time corresponding to the sub-source with maximum slip rate. Red line represents the fit, of which the slope gives a velocity rupture of  $2.4 \pm 0.3$  km/s.

## 6 Conclusions and perspectives

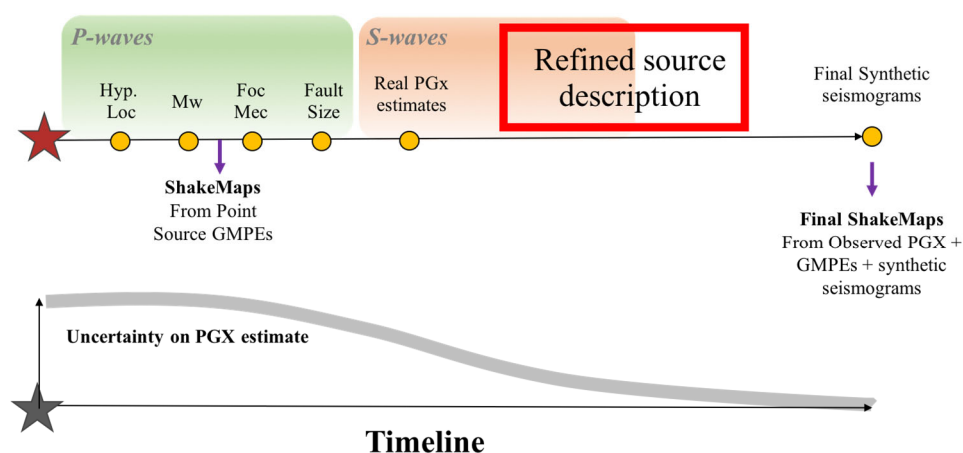


Figura Fehler! Verwenden Sie die Registerkarte 'Start', um 0 dem Text zuzuweisen, der hier angezeigt werden soll.5.1: Schematic description of some of the WP 28 activities and objectives. (top) At the occurrence of an event, moving on the timeline in the P-waves time window fast estimates of the hypocenter, magnitude and fault geometry are computed. During the recording of the S-wave phase, the real PGx estimates becomes available. The S-waves recording along with the previous estimates are hence used to compute refined source models with complementary approaches. Finally, these models will be used in the next activities of the project to compute refined synthetic seismograms and the final Shake Maps. (bottom) The definition of a refined source model is expected to reduce the uncertainty on the PGx estimates few minutes after the end of the event.

One of the main objectives of the SERA-Project WP28-JRA6 is the computation, over a rapid response time scale, of the expected ground motion through a new generation of shaking maps combining the information deriving from the observed Peak Ground kinematic parameters (PGx) the attenuation expected from local Ground Motion Prediction Equation (GMPEs) and synthetic seismograms deriving from physically-based seismic source description. In this framework, the goal of the task 28.3 was to investigate suitable strategies to exploit fast estimates of hypocenter, magnitude and fault geometry available during the P-wave recordings (see Report 28.1 and section 2.2) and the incoming S-wave recordings to generate stable and reliable kinematic source descriptions. These refined source models (see red square in the schematic description of figure 6.1.1, top panel) are currently being used, for the computation of refined synthetic seismograms and shake maps with the aim of reducing the PGx uncertainties.

With this regard we have presented the performance of two source inversion techniques that are expected to provide different and possibly complementary imaging of the source using different approaches. For both techniques, SLIPNEAR and the Back-Projection, we described the technical details of the algorithms and the needed data pre-processing, before presenting the performances of the method for a synthetic kinematic source model, referred to as the true model.

SLIPNEAR has been shown to work in a frequency band ranging from 0.05 and 0.14 Hz, and when a good azimuthal coverage of the network is available. This technique correctly localized the position of the main patch of the slip properly detecting the combined up-dip and NNW along-strike directivity of the true model. The maximum slip is slightly smaller than the maximum slip of the true model; however, in the  $k^{-2}$  definition of the synthetic source the maximum slip amplitude is due to the combination of a fixed low frequency asperity with several overlapping stochastic asperities at shorter wavelength. The contribution of these latter asperities cannot be retrieved at the characteristic inversion frequencies of SLIPNEAR.

SLIPNEAR allows for the automatic comparison between the analyzed data and the synthetic seismograms computed through the forward modelling of the source imaging. Despite of the use of two different velocity models for the true model and the inversion, a good agreement between the traces has been retrieved with an index of confidence of the final slip imaging of ~91%. Conversely, the index of confidence on the selection of the focal mechanism is quite low (~34%). This is due to the similarity of the along-strike extension for the two nodal planes. The rapid discrimination of the nodal plane is a crucial issue in the rapid response ground shaking prediction and it deserves further investigations. Nevertheless, for the case of the Norcia earthquake, some mechanical consideration may help to empirically unravel the issue. Indeed, for a normal faulting the low value of the dip angle for the auxiliary plane (34°) is an important hint that this solution should be weighted less in the definition of the disseminated final source imaging.

SLIPNEAR is already implemented in an automatic procedure that is triggered at the occurrence of events beyond a fixed magnitude threshold ( $M_w \geq 5.8$ ). Some of the automatic performance of the technique has been presented in this report to show the level of confidence of the solution and its agreement with other consolidated source inversion techniques. The results are currently disseminated through a message on the social network Twitter.

All the presented results have been made available over a time scale of tens of minutes after the triggering of the procedure. Although some efforts might be made to further reduce this duration, the estimated process time makes SLIPNEAR compatible with the implementation of a seismic-source ground shaking prediction system working over a rapid response time scale.

The back-projection technique is used for the location of source contributions (nucleation and arrest phases, short wavelength asperities) at higher frequency (>0.1-0.2 Hz), through the analysis of the signal coherence in narrow frequency bands. By analyzing the signal coherency in moving time window, whose duration depends on the frequency band, the back-projection also allows tracking the evolution of the slip rate in space and time hence providing estimates of other kinematic quantities such as the rise time and the rupture velocity.

We inverted the same synthetic data used for the SLIPNEAR analyses and we investigated two frequency ranges, 0.15-0.5 Hz (low frequency band) and 0.5-2.0 Hz (high frequency band). These bins are complementary each other as well as complementary to the bin used for the SLIPNEAR inversion. It is also worth to note that the low frequency band contains the estimated corner frequency for the event (~0.25 Hz)

By using all the near-source stations in the distance range 15-45 km from the hypocenter, we showed that this technique locates the main slip contributions at the boundary of the 1 m and 2.5 m isolines when we filter the data in the low and high frequency band respectively. In other words, this analysis confirmed that the back-projection is able to adequately locate the position of the phase generated by the strongest slip discontinuities at the border of the main asperities at different wavelengths. Nevertheless, for this application, the retrieved final maximum slip amplitude is quite small (tens of centimeters) and the time-space evolution of the slip rate and the rupture velocity are incompatible with the expected directivity of the true model. These inconsistencies have to be more deeply investigated, but they are possibly related to the uneven and numerically insufficient station distribution for the explored fault geometry.

By analogy with some other regional and tele-seismic previous applications (Maercklin *et al.* 2012, Satriano *et al.*, 2014) we inverted data following an array approach, that is grouping the stations as a function of their position with respect to the fault plane. The best results were obtained for the northern stations that are deployed along the directive direction of the true model. Although some spurious contributions appear on the boundary of the fault in the direction of the array, the boundary of the 1 m isoline is still retrieved, at least for the low frequency band. Moreover, the space-time evolution of the slip rate and the rupture velocity estimate are now in agreement with the true model rupture kinematics.

This work shows advantages and limitations of the two approaches and their ability to retrieve specific details of the kinematic rupture model. How the two models could be combined in order to provide a refined and complete-frequency source description has to be investigated in the future. In particular which is the best representation of the source for the prediction of peak ground motion. Further synthetic analyses in different source and station geometries are needed to understand whether BP is usable to provide the precise contouring of the high slip patches, previously determined by SLIPNEAR, or setting appropriate values of the rupture velocity for modelling.

All the presented back-projection analysis, also including the pre-processing phase has been carried out over computational time ranging from seconds to few minutes. The process can be easily implemented in an automatic procedure to be triggered once stable solutions for the hypocenter and the source geometry are available.

The approach followed in this task was to use the information on the macro-parameters of the fault (nucleation eqk location, seismic moment, focal mechanism and fault length) derived from the real-time analysis of the early P-waves, which allowed to set a preliminary location, geometry and mechanism of the fault which is used as an a priori for the following kinematic inversion. As it is represented in the schematic picture of figure 5.5.1 the entire chain of signal processing and modelling from early P-wave signals to late S-arrival can provide useful source kinematic models to be used for generating synthetic peak ground motion data to be integrated with observed ones in generating real-time shake-maps.

In conclusions we have verified how distinct approaches inverting signals filtered in different frequency bands may contribute to provide complementary information about the seismic source kinematics. For our applications, a prompt approach to combine this information is to define sets of slip distributions obtained adding the SLIPNEAR source imaging and overlapping stochastically distributed shorter wavelength slip patches following a classical  $k^{-2}$  approach (Herrero & Bernard 1994). In this approach, the back-projection may be used to constrain the boundary of the ruptured area on the fault plane and provide average estimates of rupture velocity and rise time.

Further effort will be dedicated to improve the resolution of the back-projection in the determination of the location and amplitude of the slip imaging, in particular to exploit at the same time the advantages emerged from the presented full network and array inversions. This improvement will be eventually used to constrain also the positions of the shorter wavelength slip asperities.

## 7 References

---

- Aki, K. & P. G. Richards (1980). *Quantitative Seismology: Theory and Methods*, W. H. Freeman and Company.
- Bianchi, I., Chiarabba C., Piana Agostinetti N, (2010). The 2009 L'Aquila (central Italy) earthquake rupture controlled by a high  $V_s$  barrier: A Receiver Function application. *Journal of Geophysical Research*, 115, B12326, doi:10.1029/2009JB007087.
- Böse, M., Clinton, J., Massin, F., Cauzzi, C., Smith, D., Andrews, J. (2018). Offline-Performance of FinDer v. 2 during the 2016/17 Central Italy Earthquake Sequence. *EGU General Assembly Conference Abstracts*

- Böse, M., Heaton, T. H., Hauksson, E. (2012). Real-time Finite Fault Rupture Detector (FinDer) for Large Earthquakes, *Geophysical Journal International*, 191(2), 803-812. doi:10.1111/j.1365-246X.2012.05657.x.
- Böse, M., Felizardo, C., Heaton, T. H. (2015). Finite-Fault Rupture Detector (*FinDer*): Going Real-Time in Californian *ShakeAlert* Warning System. *Seismological Research Letters*, 86 (6): 1692–1704. doi: <https://doi.org/10.1785/0220150154>
- Bouchon, M. (1981). A simple method to calculate Green's functions for elastic layered media, *Bulletin of Seismological Society Am.* 71, 959-971.
- Delouis, B., Charlety, J., Vallée, M., (2009). Rapid determination of moment magnitude  $M_w$  for moderate to large earthquakes from the near-field spectra of strong-motion records (MWSYNTH), in *Bulletin of the Seismological Society of America*, 99, 1827–1840, doi: 10.1785/0120080234
- Delouis, B., (2014). FMNEAR: determination of focal mechanism and first estimate of rupture directivity using near source records and a linear distribution of point sources, *Bulletin of the Seismological Society of America*, 104 (3), 1479-1500. doi: 10.1785/0120130151
- Festa, G., & Zollo, A., (2006). Fault slip and rupture velocity inversion by isochrone backprojection, *Geophysical Journal International*, Volume 166, Issue 2, August 2006, Pages 745–756, <https://doi.org/10.1111/j.1365-246X.2006.03045.x>
- Herrero A., & Bernard, P. (1996). Modeling Directivity of Heterogeneous Earthquake Ruptures. *Bulletin of the Seismological Society of America*, 86(4), 1149–1160.
- Ishii, M., (2011). High-frequency rupture properties of the  $M_w$  9.0 off the Pacific Coast of Tohoku Earthquake. *Earth, Planets, and Space* 63, 609-614.
- Maercklin, N., Festa, G., Colombelli, S., Zollo, A., (2012). “Twin ruptures grew to build up the giant 2011 Tohoku, Japan, earthquake.” *Scientific reports* vol. 2: 709. doi:10.1038/srep00709
- Nazeri, S., Colombelli, S., Zollo, A., (2019). Fast and accurate determination of earthquake moment, rupture length and stress release for the 2016–2017 Central Italy seismic sequence, *Geophysical Journal International*, Volume 217, Issue 2, May 2019, Pages 1425–1432, <https://doi.org/10.1093/gji/ggz097>
- Spudich, P. & Cranswick, E. (1984). Direct observation of rupture propagation during the 1979 Imperial Valley earthquake using a short baseline accelerometer array. *Bulletin of the Seismological Society of America* ; 74 (6): 2083–2114.
- Pizzi, A., Di Domenica, A., Gallovič, F., Luzi, L., & Puglia, R. (2017). Fault segmentation as constraint to the occurrence of the main shocks of the 2016 Central Italy seismic sequence. *Tectonics*, 36. <https://doi.org/10.1002/2017TC004652>
- Satriano, C., Dionicio, V., Miyake, H., Uchida, N., Vilotte, JP., Bernard, B. (2014). Structural and thermal control of seismic activity and megathrust rupture dynamics in subduction zones: Lessons from the  $M_w$  9.0, 2011 Tohoku earthquake, *Earth and Planetary Science Letters*, Volume 403, Pages 287-298, ISSN 0012-821X, <https://doi.org/10.1016/j.epsl.2014.06.037>.

Scala, A., G. Festa, S. Del Gaudio, S. (2018). Relation Between Near-Fault Ground Motion Impulsive Signals and Source Parameters. *Journal of Geophysical Research* , 123, 9, 7707-7721, [doi: 10.1029/2018JB015635](https://doi.org/10.1029/2018JB015635).

Scognamiglio, L., Tinti, E., Casarotti, E., Pucci, S., Villani, F., Cocco, M., et al. (2018). Complex fault geometry and rupture dynamics of the MW 6.5, 30 October 2016, central Italy earthquake. *Journal of Geophysical Research: Solid Earth*, 123, 2943–2964. <https://doi.org/10.1002/2018JB015603>

Suzuki, W., Pulido, N., Aoi, S., (2016). Rupture Process and Strong-Motion Generation of the 2014 Iquique, Northern Chile, Earthquake. *Journal of Earthquake and Tsunami* 1783-7116

Tarantino, S. Colombelli, S., Emolo, A., Zollo, A. (2019). Quick Determination of the Earthquake Focal Mechanism from the Azimuthal Variation of the Initial *P*-Wave amplitude. *Seismological Research Letters*, 90 (4): 1642–1649. doi: <https://doi.org/10.1785/0220180290>

Wells, D.L., & Coppersmith, K.J., (1994). New empirical relationships among magnitude, rupture length, rupture width, rupture area, and surface displacement: *Bulletin of the Seismological Society of America*, v. 84, no. 4, p. 974–1002

#### Liability claim

The European Union and its Innovation and Networks Executive Agency (INEA) are not responsible for any use that may be made of the information any communication activity contains.

The content of this publication does not reflect the official opinion of the European Union. Responsibility for the information and views expressed in the therein lies entirely with the author(s).